Search for astrophysical neutrino-induced cascades with IceCube-40

R. Abbasi,[28] Y. Abdou,[23] T. Abu-Zayyad,[34] M. Ackermann,[42] J. Adams,[16] J. A. Aguilar,[22] M. Ahlers,[28] D. Altmann,[9] K. Andeen,[28] J. Auffenberg,[28] X. Bai,[32,*] M. Baker,[28] S. W. Barwick,[24] V. Baum,[29] R. Bay,[7] K. Beattie,[8] J. J. Beatty,[18,19] S. Bechet,[13] J. Becker Tjus,[10] K.-H. Becker,[41] M. Bell,[39] M. L. Benabderrahmane,[42] S. BenZvi,[28] J. Berdermann,[42] P. Berghaus,[42] D. Berley,[17] E. Bernardini,[42] D. Bertrand,[13] D. Z. Besson,[26] D. Bindig,[41] M. Bissok,[1] E. Blaufuss,[17] J. Blumenthal,[1] D. J. Boersma,[1] C. Bohm,[35] D. Bose,[14] S. Böser,[11] O. Botner,[40] L. Brayeur,[14] A. M. Brown,[16] R. Bruijn,[25] J. Brunner,[42] S. Buitink,[14] K. S. Caballero-Mora,[39] M. Carson,[23] J. Casey,[5] M. Casier,[14] D. Chirkin,[28] B. Christy,[17] F. Clevermann,[20] S. Cohen,[25] D. F. Cowen,[39,38] A. H. Cruz Silva,[42] M. Danninger,[35] J. Daughhetee,[5] J. C. Davis,[18] C. De Clercq,[14] F. Descamps,[28] P. Desiati,[28] G. de Vries-Uiterweerd,[23] T. DeYoung,[39] J. C. Díaz-Vélez,[28] J. Dreyer,[10] J. P. Dumm,[28] M. Dunkman,[39] R. Eagan,[39] J. Eisch,[28] R. W. Ellsworth,[17] O. Engdegård,[40] S. Euler,[1] P. A. Evenson,[32] O. Fadiran,[28] A. R. Fazely,[6] A. Fedynitch,[10] J. Feintzeig,[28] T. Feusels,[23] K. Filimonov,[7] C. Finley,[35] T. Fischer-Wasels,[41] S. Flis,[35] A. Franckowiak,[11] R. Franke,[42] K. Frantzen,[20] T. Fuchs,[20] T. K. Gaisser,[32] J. Gallagher,[27] L. Gerhardt,[8,7] L. Gladstone,[28] T. Glüsenkamp,[42] A. Goldschmidt,[8] J. A. Goodman,[17] D. Góra,[42] D. Grant,[21] A. Groß,[31] S. Grullon,[28] M. Gurtner,[41] C. Ha,[8,7] A. Haj Ismail,[23] A. Hallgren,[40] F. Halzen,[28] K. Hanson,[13] D. Heereman,[13] P. Heimann,[1] D. Heinen,[1] K. Helbing,[41] R. Hellauer,[17] S. Hickford,[16,†] G. C. Hill,[2] K. D. Hoffman,[17] R. Hoffmann,[41] A. Homeier,[11] K. Hoshina,[28] W. Huelsnitz,[17,‡] P. O. Hulth,[35] K. Hultqvist,[35] S. Hussain,[32] A. Ishihara,[15] E. Jacobi,[42] J. Jacobsen,[28] G. S. Japaridze,[4] O. Jlelati,[23] H. Johansson,[35] A. Kappes,[9] T. Karg,[42] A. Karle,[28] J. Kiryluk,[36] F. Kislat,[42] J. Kläs,[41] S. R. Klein,[8,7] J.-H. Köhne,[20] G. Kohnen,[30] H. Kolanoski,[9] L. Köpke,[29] C. Kopper,[28] S. Kopper,[41] D. J. Koskinen,[39] M. Kowalski,[11] M. Krasberg,[28] G. Kroll,[29] J. Kunnen,[14] N. Kurahashi,[28] T. Kuwabara,[32] M. Labare,[14] K. Laihem,[1] H. Landsman,[28] M. J. Larson,[37] R. Lauer,[42] M. Lesiak-Bzdak,[36] J. Lünemann,[29] J. Madsen,[34] R. Maruyama,[28] K. Mase,[15] H. S. Matis,[8] F. McNally,[28] K. Meagher,[17] M. Merck,[28] P. Mészáros,[38,39] T. Meures,[13] S. Miarecki,[7,8] E. Middell,[42] N. Milke,[20] J. Miller,[14] L. Mohrmann,[42] T. Montaruli,[22,§] R. Morse,[28] S. M. Movit,[38] R. Nahnhauer,[42] U. Naumann,[41] S. C. Nowicki,[21] D. R. Nygren,[8] A. Obertacke,[41] S. Odrowski,[31] A. Olivas,[17] M. Olivo,[10] A. O'Murchadha,[13] S. Panknin,[11] L. Paul,[1] J. A. Pepper,[37] C. Pérez de los Heros,[40] D. Pieloth,[20] N. Pirk,[42] J. Posselt,[41] P. B. Price,[7] G. T. Przybylski,[8] L. Rädel,[1] K. Rawlins,[3] P. Redl,[17] E. Resconi,[31] W. Rhode,[20] M. Ribordy,[25] M. Richman,[17] B. Riedel,[28] J. P. Rodrigues,[28] F. Rothmaier,[29] C. Rott,[18] T. Ruhe,[20] D. Rutledge,[39] B. Ruzybayev,[32] D. Ryckbosch,[23] T. Salameh,[39] H.-G. Sander,[29] M. Santander,[28] S. Sarkar,[33] S. M. Saba,[10] K. Schatto,[29] M. Scheel,[1] F. Scheriau,[20] T. Schmidt,[17] M. Schmitz,[20] S. Schoenen,[1] S. Schöneberg,[10] L. Schönherr,[1] A. Schönwald,[42] A. Schukraft,[1] L. Schulte,[11] O. Schulz,[31] M. Schunck,[1] D. Seckel,[32] S. H. Seo,[35] Y. Sestayo,[31] S. Seunarine,[12] M. W. E. Smith,[39] M. Soiron,[1] D. Soldin,[41] G. M. Spiczak,[34] C. Spiering,[42] M. Stamatikos,[18,¶] T. Stanev,[32] A. Stasik,[11] T. Stezelberger,[8] R. G. Stokstad,[8] A. Stößl,[42] E. A. Strahler,[14] R. Ström,[40] G. W. Sullivan,[17] H. Taavola,[40] I. Taboada,[5] A. Tamburro,[32] S. Ter-Antonyan,[6] S. Tilav,[32] P. A. Toale,[37] S. Toscano,[28] M. Usner,[11] N. van Eijndhoven,[14] D. Van Der Drift,[8,7] A. Van Overloop,[23] J. van Santen,[28] M. Vehring,[1] M. Voge,[11] C. Walck,[35] T. Waldenmaier,[9] M. Wallraff,[1] M. Walter,[42] R. Wasserman,[39] Ch. Weaver,[28] C. Wendt,[28] S. Westerhoff,[28] N. Whitehorn,[28] K. Wiebe,[29] C. H. Wiebusch,[1] D. R. Williams,[37] H. Wissing,[17] M. Wolf,[35] T. R. Wood,[21] K. Woschnagg,[7] C. Xu,[32] D. L. Xu,[37] X. W. Xu,[6] J. P. Yanez,[42] G. Yodh,[24] S. Yoshida,[15] P. Zarzhitsky,[37] J. Ziemann,[20] A. Zilles,[1] and M. Zoll[35]

(IceCube Collaboration)

[1] *III. Physikalisches Institut, RWTH Aachen University, D-52056 Aachen, Germany*
[2] *School of Chemistry & Physics, University of Adelaide, Adelaide SA, 5005 Australia*
[3] *Dept. of Physics and Astronomy, University of Alaska Anchorage, 3211 Providence Dr., Anchorage, AK 99508, USA*
[4] *CTSPS, Clark-Atlanta University, Atlanta, GA 30314, USA*
[5] *School of Physics and Center for Relativistic Astrophysics, Georgia Institute of Technology, Atlanta, GA 30332, USA*
[6] *Dept. of Physics, Southern University, Baton Rouge, LA 70813, USA*
[7] *Dept. of Physics, University of California, Berkeley, CA 94720, USA*
[8] *Lawrence Berkeley National Laboratory, Berkeley, CA 94720, USA*
[9] *Institut für Physik, Humboldt-Universität zu Berlin, D-12489 Berlin, Germany*
[10] *Fakultät für Physik & Astronomie, Ruhr-Universität Bochum, D-44780 Bochum, Germany*
[11] *Physikalisches Institut, Universität Bonn, Nussallee 12, D-53115 Bonn, Germany*
[12] *Dept. of Physics, University of the West Indies, Cave Hill Campus, Bridgetown BB11000, Barbados*

[13] Université Libre de Bruxelles, Science Faculty CP230, B-1050 Brussels, Belgium
[14] Vrije Universiteit Brussel, Dienst ELEM, B-1050 Brussels, Belgium
[15] Dept. of Physics, Chiba University, Chiba 263-8522, Japan
[16] Dept. of Physics and Astronomy, University of Canterbury, Private Bag 4800, Christchurch, New Zealand
[17] Dept. of Physics, University of Maryland, College Park, MD 20742, USA
[18] Dept. of Physics and Center for Cosmology and Astro-Particle Physics, Ohio State University, Columbus, OH 43210, USA
[19] Dept. of Astronomy, Ohio State University, Columbus, OH 43210, USA
[20] Dept. of Physics, TU Dortmund University, D-44221 Dortmund, Germany
[21] Dept. of Physics, University of Alberta, Edmonton, Alberta, Canada T6G 2G7
[22] Département de physique nucléaire et corpusculaire, Université de Genève, CH-1211 Genève, Switzerland
[23] Dept. of Physics and Astronomy, University of Gent, B-9000 Gent, Belgium
[24] Dept. of Physics and Astronomy, University of California, Irvine, CA 92697, USA
[25] Laboratory for High Energy Physics, École Polytechnique Fédérale, CH-1015 Lausanne, Switzerland
[26] Dept. of Physics and Astronomy, University of Kansas, Lawrence, KS 66045, USA
[27] Dept. of Astronomy, University of Wisconsin, Madison, WI 53706, USA
[28] Dept. of Physics and Wisconsin IceCube Particle Astrophysics Center, University of Wisconsin, Madison, WI 53706, USA
[29] Institute of Physics, University of Mainz, Staudinger Weg 7, D-55099 Mainz, Germany
[30] Université de Mons, 7000 Mons, Belgium
[31] T.U. Munich, D-85748 Garching, Germany
[32] Bartol Research Institute and Department of Physics and Astronomy, University of Delaware, Newark, DE 19716, USA
[33] Dept. of Physics, University of Oxford, 1 Keble Road, Oxford OX1 3NP, UK
[34] Dept. of Physics, University of Wisconsin, River Falls, WI 54022, USA
[35] Oskar Klein Centre and Dept. of Physics, Stockholm University, SE-10691 Stockholm, Sweden
[36] Department of Physics and Astronomy, Stony Brook University, Stony Brook, NY 11794-3800, USA
[37] Dept. of Physics and Astronomy, University of Alabama, Tuscaloosa, AL 35487, USA
[38] Dept. of Astronomy and Astrophysics, Pennsylvania State University, University Park, PA 16802, USA
[39] Dept. of Physics, Pennsylvania State University, University Park, PA 16802, USA
[40] Dept. of Physics and Astronomy, Uppsala University, Box 516, S-75120 Uppsala, Sweden
[41] Dept. of Physics, University of Wuppertal, D-42119 Wuppertal, Germany
[42] DESY, D-15735 Zeuthen, Germany

(Dated: August 27, 2012)

We report on the search for astrophysical neutrino-induced cascades in the IceCube detector. The data for this search were collected between April 2008 and May 2009 when the first 40 IceCube strings were deployed and operational. We observed fourteen cascade candidate events after event selection, on an expected background of $4.3^{+1.1}_{-1.0}$ atmospheric neutrino events and 7.7 ± 1.0 atmospheric muon events. At a 90% confidence level we set an all-flavour upper limit of $\Phi_{\rm lim} \mathrm{E}^2 \leq 5.21 \times 10^{-8}\,\mathrm{GeV sr^{-1} s^{-1} cm^{-2}}$ on the diffuse flux from astrophysical neutrinos for the energy range 25 TeV to 5012 TeV, assuming an E_ν^{-2} spectrum and a neutrino flavour ratio of 1 : 1 : 1 at the Earth.

I. INTRODUCTION

The sources of the highest energy cosmic-rays are unknown. Astrophysical objects targeted as possible sources include supernova remnants, active galactic nuclei, gamma-ray bursts, and core collapse supernova. High energy neutrino production is predicted to occur in regions of the universe where cosmic-rays are accelerated. Cosmic-ray protons are expected to interact with ambient protons or photons surrounding their acceleration site[30]. Although to date no astrophysical sources of neutrinos have been conclusively identified, analyses searching for them have established limits enabling astrophysical models to be constrained.

Fermi acceleration of charged particles in magnetic shocks followed by collisions with matter or radiation between the astrophysical source and the Earth leads to a harder energy spectrum for astrophysical neutrinos than that arising from atmospheric neutrinos, typically close to an E_ν^{-2} spectrum. Due to oscillations neutrinos from meson decay sources arrive at the Earth with a flavour ratio of approximately $\nu_\tau : \nu_\mu : \nu_e = 1 : 1 : 1$[12, 14]. The astrophysical neutrino flux is not known but is expected to be lower than the Waxman-Bahcall upper bound[43].

Diffuse analyses search for an all-sky neutrino flux. If

*Physics Department, South Dakota School of Mines and Technology, Rapid City, SD 57701, USA
†Corresponding author: stephanie.hickford@pg.canterbury.ac.nz
‡Los Alamos National Laboratory, Los Alamos, NM 87545, USA
§also Sezione INFN, Dipartimento di Fisica, I-70126, Bari, Italy
¶NASA Goddard Space Flight Center, Greenbelt, MD 20771, USA

there are numerous astrophysical sources with unobservably low fluxes the aggregate flux may still be observable as a diffuse flux. A cascade analysis searches for the signature of a neutrino-induced particle shower. Cascades arise from the interaction of all three active flavours of neutrinos; the charged-current electron-neutrino interaction and the neutral-current electron-, muon-, and tau-neutrino interactions.

The IceCube neutrino detector observes the Cherenkov radiation from secondary charged particles produced in neutrino-nucleon interactions in the medium. The Cherenkov radiation is recorded by an optical sensor array deployed in the ice at the South Pole. Track events initiated by particles such as muons are observed as a cone of Cherenkov light traveling through the detector at speeds close to c, while cascade events are appear as point-like Cherenkov emitters over a small region in the ice.

An advantage of a cascade search over a muon search is that cascade events have superior energy resolution. This is particularly important for diffuse searches which use a change in the spectral shape to recognise the presence of an astrophysical neutrino flux on top of the atmospheric neutrino background. The superior energy resolution for cascade events is due to the fact that cascades deposit their energy within a small spatial region, while muons deposit energy over their entire track length.

Previous diffuse searches have been performed using muons[4] and all-flavour cascades[6], yielding results consistent with the background prediction and have set limits on astrophysical neutrino models.

This paper presents the diffuse cascade search for astrophysical neutrino-induced cascades in the 40-string IceCube detector. In section II the IceCube detector and IceCube-40 dataset is described. In section III the simulation of signal and background events is described, the event selection criteria is outlined, and the systematic uncertainties to the analysis is presented. In section IV the results from the cascade analysis is presented and section V concludes the work.

II. THE ICECUBE DETECTOR

IceCube is the first kilometre-scale Cherenkov neutrino telescope. IceCube consists of optical sensors, called *Digital Optical Modules* (DOMs)[2], designed to detect Cherenkov photons produced by secondary particles from neutrino-nucleon interactions occurring within the ice. The DOMs are deployed between depths of 1450 m and 2450 m on 40 strings lowered into the ice. Each string has 60 DOMs attached that are optically coupled to the surrounding ice. The vertical spacing of the DOMs on each string is approximately 17 m and the horizontal spacing between the strings is approximately 125 m.

On board each DOM is a 25 cm diameter R7081-02 *PhotoMultiplier Tube* (PMT)[3], made by Hamamatsu Photonics, and a data acquisition system housed within a pressure sphere made of 13 mm thick borosilicate glass. The PMTs dynamic range is 200 photoelectrons per 15 ns and it is designed to accurately record the amplitudes and widths of the pulses with a timing resolution of 5 ns. Their peak quantum efficiency is approximately 25 % and are operated at a gain of 10^7.

The data acquisition system records the arrival times of the detected photoelectrons from Cherenkov radiation. The DOM mainboard is 274 mm in diameter and contains the central processor that receives signals from the PMT. High-bandwidth waveform capture is accomplished by an *Application Specific Integrated Circuit* (ASIC) including an *Analog-to-digital Transient Waveform Digitizer* (ATWD) and a *flash Analog-to-Digital Converter* (fADC). The ATWDs provide a sampling rate of 300 MHz over a time window of 450 ns. The ATWDs have four channels, each storing 128 samples with 10 bit resolution. One channel is used for flasher runs and calibration, while the other three channels have various gains which are used to digitize the PMT output. The fADC has a coarser sampling of 40 MHz and records data over a longer time period of up to 6.4 µs. The PMTs produce time-stamped digitized signal waveforms which are transmitted to the surface for analysis.

The data for this cascade analysis was collected between April 2008 and May 2009 when 40 of the IceCube strings were deployed and operational. Figure 1 shows the IceCube-40 detector configuration where the point $(x, y, z) = (0, 0, 0)$ is the centre of the complete 86-string detector.

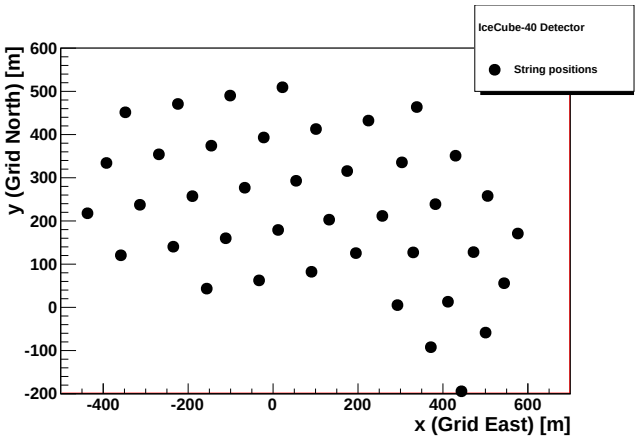

FIG. 1: The IceCube-40 detector configuration. The filled circles are the positions of the strings in the xy-coordinate system.

The trigger requirement for the IceCube-40 cascade physics stream was the *Simple Multiplicity Trigger* (SMT), which required that eight DOMs were hit within a 5000 ns time window. A waveform of photons verses time was produced for the event. The hit was sent to the surface of the detector if the local coincidence criteria were met. Local coincidence required a neighbouring DOM on the same string, either one DOM above

or one DOM below, also detecting light within the local coincidence time window of ±1000 ns. The data rate for IceCube-40 from the trigger level was approximately 1500 Hz.

III. ANALYSIS

After the trigger condition the backgrounds arising from atmospheric muons and atmospheric neutrinos remained many orders of magnitude above the rate of neutrino-induced cascades expected from astrophysical sources. This analysis consisted of a series of cuts, called filtering levels, on reconstructed event variables designed to distinguish between background events and signal events. Filtering cuts were developed using the simulation and a sample of 10% of the data. The remaining 90% of the data was blinded until all cuts were finalised so that classifications of events were free from bias. Section III A describes the simulated datasets used to develop filtering cuts, section III B describes filter levels 3 to 6, and section III C describes the systematic uncertainties associated with the analysis.

A. Simulation

Interactions of all flavours of neutrinos were simulated to model neutrino signal and background. The simulation program used, based on the program *All Neutrino Interaction Simulation* (ANIS)[26], produces neutrinos isotropically over the Earths surface and propagates them to interact in or near the detector volume. The CTEQ 5 model was used for the neutrino cross-sections. The neutrino background for this search is from atmospheric neutrinos, assumed to arise from the Bartol model[13] for conventional atmospheric neutrinos and the Sarcevic model[21] for prompt atmospheric neutrinos.

The dominant background in this analysis came from atmospheric muons that were created in air showers due to cosmic-ray interactions in the Earths atmosphere. These air showers were simulated using Monte Carlo techniques with a modified version[17, 18] of *COsmic Ray SImulations for KAscade* (CORSIKA)[28]. The interaction models used are Gheisha and QGSJET-II, and primary energy spectra were simulated from the polygonato model[32] and the two-component Glasstetter model[27]. The polygonato model uses different energy spectra according to the primary element of the cosmic-ray. The elements are grouped by atomic mass and six different energy spectra were simulated. The polygonato model assumed cosmic-rays are composed of all elements up to uranium. However, CORSIKA only simulates cosmic-ray primaries up to iron. Elements beyond iron start to contribute to the cosmic-ray spectrum above primary energies of approximately 50 PeV and this fraction of the cosmic-ray flux is ignored in polygonato CORSIKA simulations. The most challenging background to simulate in a high-energy cascade analysis is the highest energy muons arising from high-energy cosmic-rays. In order to overcome this problem the highest energy events are oversampled via weighting. For these simulations the Glasstetter model was used, which assumes the cosmic-ray flux is composed of only proton and iron elements. The energy spectra of these elements was fitted to data taken from the *KArlsruhe Shower Core and Array DEtector* (KASCADE) array[27].

The propagation of muons and taus through the detector and their energy losses were simulated using a program called *Muon Monte Carlo* (MMC)[16]. The cascade simulation inside the detector was handled by the *Cascade Monte Carlo* (CMC)[41] program. For low-energy cascades of less than 1 TeV the event was treated as an anisotropic point source. For high-energy cascades, of greater than 1 TeV, the event was split into several smaller cascades along the longitudinal direction of the cascade.

The optical properties of the ice at the South Pole vary with depth. Within a fixed wavelength range the ice properties are described by two parameters; the effective scattering length and the absorption length. Photon propagation was simulated using PHOTONICS, a photon tracking Monte Carlo package[36] that assumes a planar ice structure. PHOTONICS calculated the photon flux and time distributions in the ice surrounding the light source[35] for muon and cascade events. Once photons have been propagated using PHOTONICS the DOM electronic response was simulated, accounting for DOM-to-DOM variations such as their orientation, and the probability of photon detection was calculated given each DOM detection efficiency.

B. Event Selection

The event selection for this analysis consists of a series of cuts performed on reconstructed event variables designed to distinguish between the background events and signal events. The reconstructed event variables seek to describe the physical quantities related to the neutrino which is assumed to have initiated the event. Quantities are calculated to describe the light distribution observed within the detector. These quantities can be used to determine the topological parameters of the event to distinguish between signal and background. Level 1, the trigger condition, was described earlier. Level 2, the online pole filter, and beyond are described in this section.

Data received after the trigger condition was satisfied was dominated by atmospheric muon background. An online filter performed on the data reduced this background while retaining the majority of the neutrino signal for more sophisticated processing. The pole filter consisted of two cuts, the line-fit velocity and the tensor of inertia eigenvalue ratio. The pole filter reduced the data rate by two orders of magnitude to approximately 16 Hz.

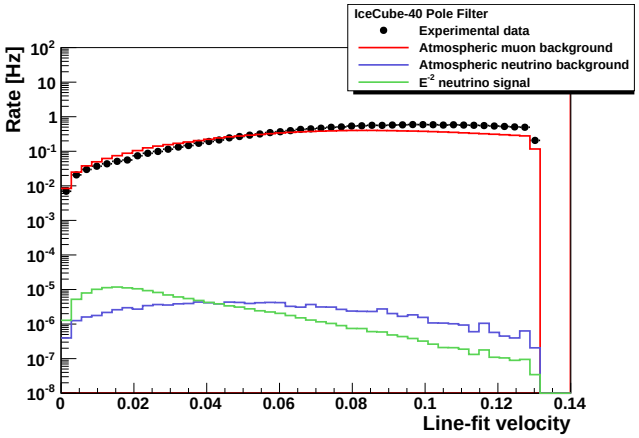

(a) Line-fit velocity < 0.13.

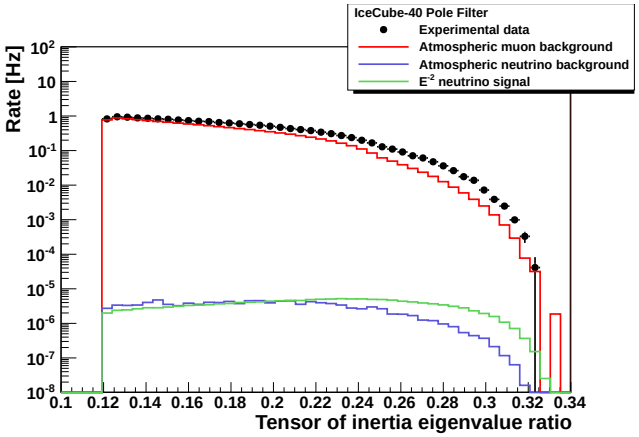

(b) Eigenvalue ratio > 0.12.

FIG. 2: The IceCube-40 pole filter, the data is shown by the black filled circles, simulated atmospheric muon background by the red line, simulated atmospheric electron neutrinos by the blue line, and simulated E^{-2} spectrum electron neutrino signal by the green line.

The line-fit velocity variable is a quantity which aims to characterise the speed at which the light from an event passed through the detector. A straight line was fitted to the event based on the DOM hit times. Using this fit an average speed for the event was calculated. This is the speed that the Cherenkov light appeared to travel through the detector along the direction of the fit. Cascade events were expected to have a line-fit velocity close to zero, while muon events were expected to have larger values of line-fit velocity. Figure 2(a) shows the line-fit velocity distributions for the data, simulated atmospheric muon background, simulated atmospheric electron neutrino background, and simulated E^{-2} spectrum electron neutrino signal.

Tensor of inertia is a reconstruction algorithm analogous to the classical tensor of inertia where the distribution of light detected by the DOMs plays the role of the mass distribution. The eigenvalues of the tensor associated with the light distribution corresponded to finding values for the lengths of the distributions along the three principal axes. The eigenvalue ratio is the ratio of the lowest eigenvalue to the sum of all three eigenvalues. This quantity is a measure of how spherical the light distribution is. A spherical cascade event would have all three eigenvalues equal and an eigenvalue ratio of $\frac{1}{3}$. Track-like events are elongated and so have an eigenvalue ratio approaching zero. Figure 2(b) shows the tensor of inertia eigenvalue ratio for the data, simulated atmospheric muon background, simulated atmospheric electron neutrino background, and simulated E^{-2} spectrum electron neutrino signal.

At level 3 the background is strongly peaked at lower energies. Consequently, the filter was only performed on events with a reconstructed energy of less than 10 TeV. Two cuts were performed below this energy: a cut on the reconstructed zenith direction and a cut on the reduced log-likelihood. These cuts reduced the data rate by an order of magnitude to approximately 1.8 Hz.

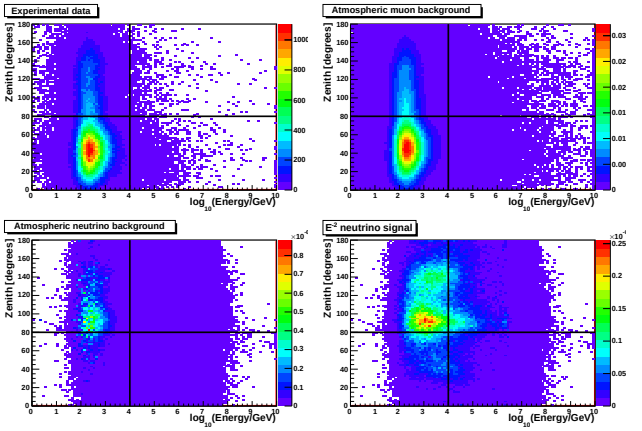

FIG. 3: The IceCube-40 level 3 zenith and energy reconstructions, the four panels show the data, atmospheric muon background, atmospheric electron neutrino background, and E^{-2} spectrum electron neutrino signal. The level 3 cuts are shown by the black lines at zenith $= 80°$ and energy $= 10$ TeV. Events in the lower left quadrant of each of the panels were removed.

The reconstructed zenith angle was calculated assuming the event had a track topology. Using this assumption the best fit to the event was found and the zenith direction of the track calculated. For events with reconstructed energies of less than 10 TeV the zenith direction cut was placed at 80° removing most track-like events that originated from above the horizon. Figure 3 shows the zenith and energy cuts for the data, simulated atmospheric muon background, simulated atmospheric electron neutrino background, and simulated E^{-2} spectrum electron neutrino signal.

The cascade log-likelihood module calculated a variable which gave the probability of observing the event hit pattern in the detector, assuming the hypothesis of a cascade event. For events with a reconstructed energy of less than 10 TeV the cut on the cascade reduced log-

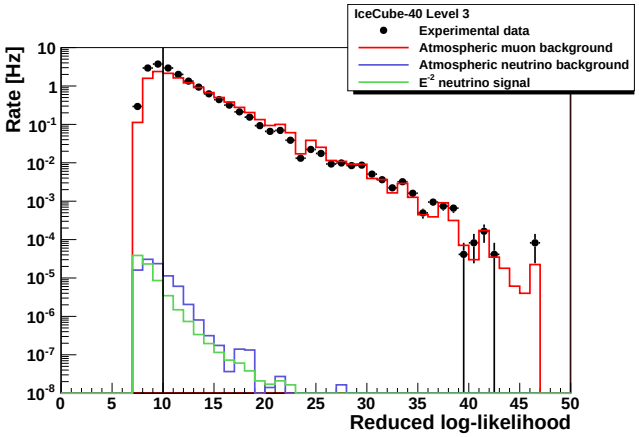

FIG. 4: The IceCube-40 level 3 filter, the data is shown by the black filled circles, simulated atmospheric muon background by the red line, simulated atmospheric electron neutrinos by the blue line, and simulated E^{-2} spectrum electron neutrino signal by the green line.

likelihood was placed at 10. Figure 4 shows the reduced log-likelihood distributions for the data, simulated atmospheric muon background, simulated atmospheric electron neutrino background, and simulated E^{-2} spectrum electron neutrino signal.

The first cut at level 4 is a cut on the energy reconstruction which was re-calculated after filter level 3. This is followed by two further cuts: a cut on the fill ratio variable and a cut on the spacial distance variable. The level 4 cuts reduced the experimental data rate by a further two orders of magnitude to 2.5×10^2 Hz.

The spatial distance variable was formed from a split reconstruction. In a split reconstruction an event is divided into two parts based on the times of the hit DOMs with each part of the event reconstructed separately. Reconstructed quantities using the first part of the hits in the event are denoted by the subscript 1 and reconstructed quantities from the second part of the hits in the event are denoted by the subscript 2. The spatial distance variable SD is the difference in the vertex position reconstruction of each part of the event and is calculated from

$$\mathrm{SD} = \sqrt{(X_2 - X_1)^2 + (Y_2 - Y_1)^2 + (Z_2 - Z_1)^2}. \quad (1)$$

If the event was a cascade event, and hence had a spherical hit topology, the vertex positions from each part of the event should reconstruct to the same location in the detector. If the event was a background muon event and hence had a track-like topology, the vertex positions from each part of the event should reconstruct to different locations in the detector. The cut on the spatial distance variable was placed at 40 m. Events with their two vertices reconstructed more than 40 m apart are removed from the event selection. Figure 5(b) shows the spacial distance distributions for the data, simulated atmospheric muon background, simulated atmospheric electron neutrino background, and simulated E^{-2} spectrum electron neutrino signal.

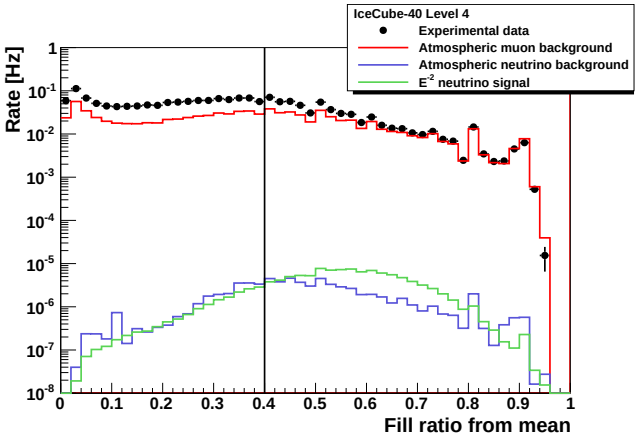

(a) Fill ratio from mean > 0.4.

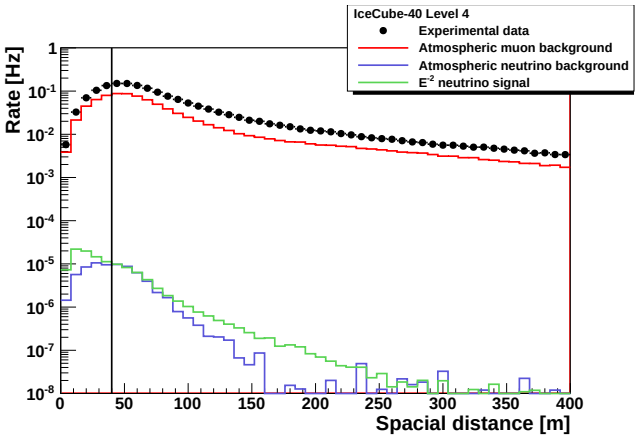

(b) Spacial distance < 40 m.

FIG. 5: The IceCube-40 level 4 filter, the data is shown by the black filled circles, simulated atmospheric muon background by the red line, simulated atmospheric electron neutrinos by the blue line, and simulated E^{-2} spectrum electron neutrino signal by the green line.

In the calculation of the fill ratio variable a sphere of radius D, centered on the reconstructed vertex, was defined by the average distance between each DOM hit in the event and the reconstructed event vertex. The fill ratio variable is the ratio of the number of hit DOMs within this sphere to the total number of DOMs within the sphere. If the event was a cascade event, and hence had near-spherical topology, the fill ratio should be close to one. If the event was track-like the fill ratio will be much less than one. The cut on fill ratio variable was placed at 0.4. Figure 5(a) shows the fill ratio distributions for the data, simulated atmospheric muon background, simulated atmospheric electron neutrino background, and simulated E^{-2} spectrum electron neutrino signal.

At level 5 containment cuts were performed. Containment cuts are necessary because the background events

which survived to this filter level are cascade-like and are mostly at the edges of the detector. The first containment cut performed was on the reconstructed z-vertex position of the event, the following two containment cuts were performed on the xy-event position. The containment cuts reduced the experimental data rate by another order of magnitude to 2.1×10^{-3} Hz.

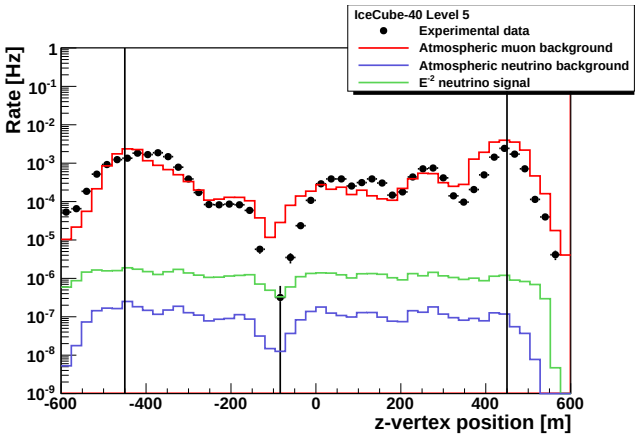

FIG. 6: The IceCube-40 level 5 depth containment filter, the data is shown by the black filled circles, simulated atmospheric muon background by the red line, simulated electron atmospheric electron neutrinos by the blue line, and simulated E^{-2} spectrum electron neutrino signal by the green line.

The cut on the reconstructed z-vertex position was placed at -450 m and at 450 m. This removed events that were reconstructed within 50 m of the top and bottom boundaries of the detector. Figure 6 shows the reconstructed z-vertex position distributions for the data, simulated atmospheric muon background, simulated atmospheric electron neutrino background, and simulated E^{-2} spectrum electron neutrino signal.

There were two containment cuts on the xy-event position. The first, called string containment, was on the events reconstructed xy-vertex . This cut required the vertex position to be reconstructed inside the outer ring of strings. This requirement excluded string 21 because it formed a sharp point in the detector layout in which a lot of background was reconstructed due to muons passing nearby without depositing light in other parts of the detector. The second xy-containment cut, called DOM charge containment, is concerned with the DOM that measures the largest deposited charge. This cut required that the DOM with the largest deposited charge be located on an inner string. The boundary of the string containment cut and the effect of these containment cuts is shown in Figures 7(a)–7(c). These Figures show the xy-coordinate system for the data, simulated atmospheric muon background, simulated atmospheric electron neutrino background, and simulated E^{-2} spectrum electron neutrino signal. The effect of each containment cut is shown by the distribution of the reconstructed vertex positions. Figure 7(a) shows the distribution of the reconstructed vertex positions before either xy-containment

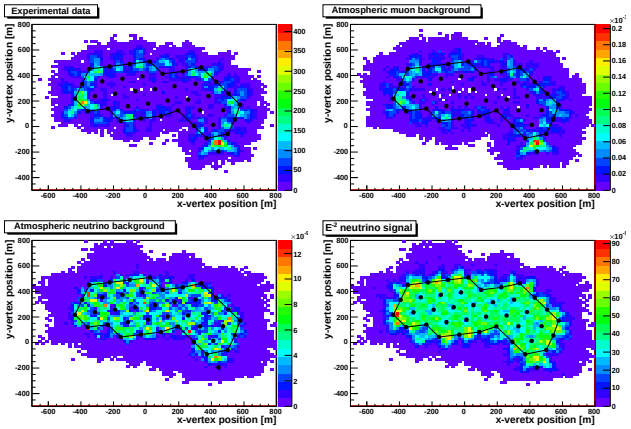

(a) Before any xy-containment cuts were performed.

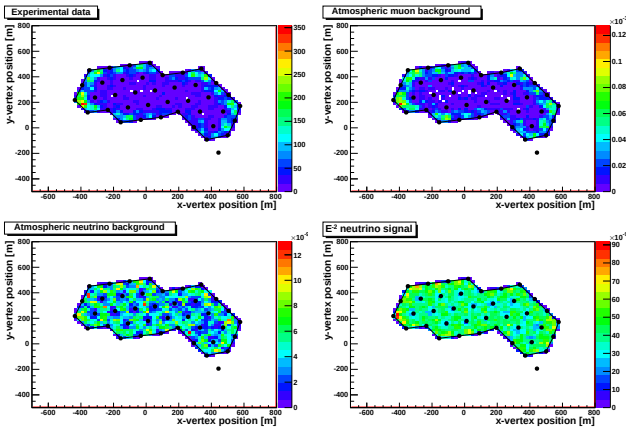

(b) After events that do not satisfy the string containment cut were removed.

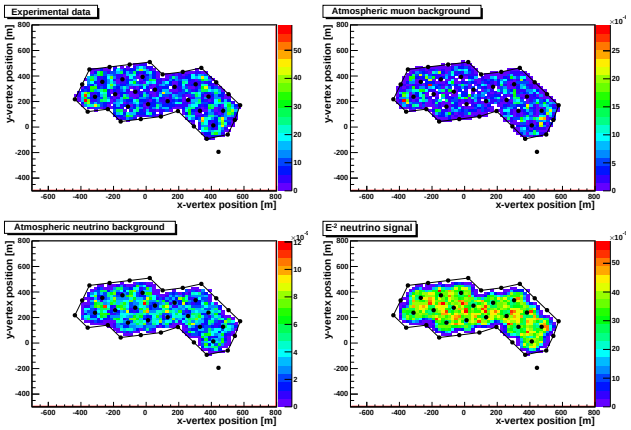

(c) After events that do not satisfy either the string containment cut or the DOM charge containment cut were removed.

FIG. 7: The IceCube-40 level 5 containment filter, the four panels show the reconstructed xy-vertex positions for the data, atmospheric muon background, atmospheric electron neutrino background, and E^{-2} spectrum electron neutrino signal.

cut, Figure 7(b) shows the distribution of the reconstructed vertex positions after the string containment cut and Figure 7(c) shows the distribution of the reconstructed vertex positions after the string containment cut and the DOM charge containment cut.

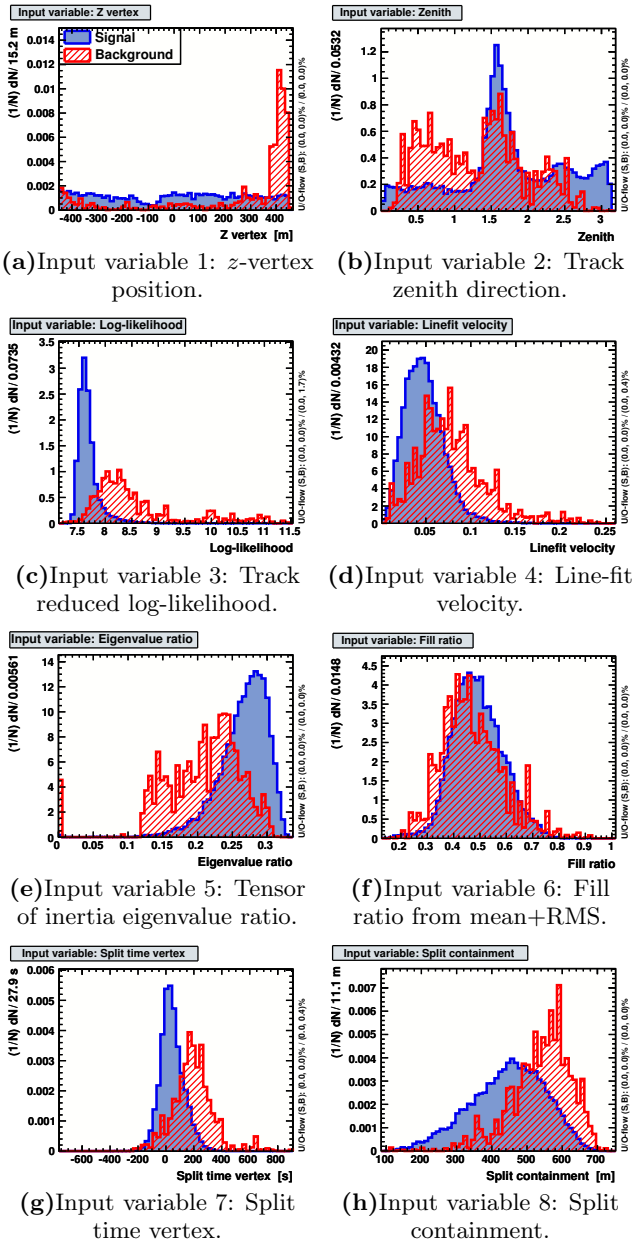

(a) Input variable 1: z-vertex position.

(b) Input variable 2: Track zenith direction.

(c) Input variable 3: Track reduced log-likelihood.

(d) Input variable 4: Line-fit velocity.

(e) Input variable 5: Tensor of inertia eigenvalue ratio.

(f) Input variable 6: Fill ratio from mean+RMS.

(g) Input variable 7: Split time vertex.

(h) Input variable 8: Split containment.

FIG. 8: The eight input variables that were fed into the TMVA algorithm to produce the BDT response score. The BDT response score had much greater separation power of background and signal than these variables do individually.

After the containment cuts were performed the background and signal were fed into a machine learning algorithm. The package used in this analysis was *Toolkit for MultiVariate Analysis* (TMVA)[31] which operates within the ROOT[15] framework. Eight variables, from atmospheric muon background simulation and E^{-2} spectrum neutrino signal simulation, were chosen for the TMVA algorithm. A training phase was performed, using half of the simulation as input, where the algorithm learned the different characteristics of the eight variables for background and signal. A testing phase was then performed using the other half of the simulation where it checked, based on the learning from the training phase, that it could correctly characterise an event as background or signal. The final output from TMVA was a variable called the BDT response[31] where the boosting algorithm used was AdaBoost[24]. This variable is the score that each event was assigned depending on how background-like or signal-like TMVA has determined the event to be. The final phase of TMVA was the evaluation phase. This was run on the data, and the background and signal simulation that were not used in the training or testing phases. The BDT response score had a strong separation power between background and signal, and gave a better separation than could be achieved using the variables individually. The eight variables fed to the TMVA algorithm are

- z-vertex position
- Track zenith direction
- Track reduced log-likelihood
- Line-fit velocity
- Tensor of inertia eigenvalue ratio
- Fill ratio from mean+RMS
- Split time vertex
- Split containment

These variables are shown, as assessed by TMVA, in Figures 8(a)–8(h). The background is shown in red and the signal in blue. The background and signal are scaled so that they are normalised to each other, although at this level the rate of the signal was still far below that of the background.

Level 6 is the final analysis filter level. It consisted of a cut on the BDT response and a cut on the energy. These cuts were optimised based on the sensitivity and discovery potential using the Feldman-Cousins method[23]. The level 6 cuts reduced the experimental data by a further four orders of magnitude to 6.4×10^{-7} Hz. The background rate at this level was below that estimated for the signal and the data could be unblinded.

To optimise the final level of cuts the experimental data was used rather than the remaining muon background from simulation. This was because the available expected to muon background simulation was limited by this stage of the analysis, and therefore would not provide a robust estimation for the best values to place the final cuts. The experimental data can be used for the optimisation because most events are still expected to be from muon background events, even at this high filter level.

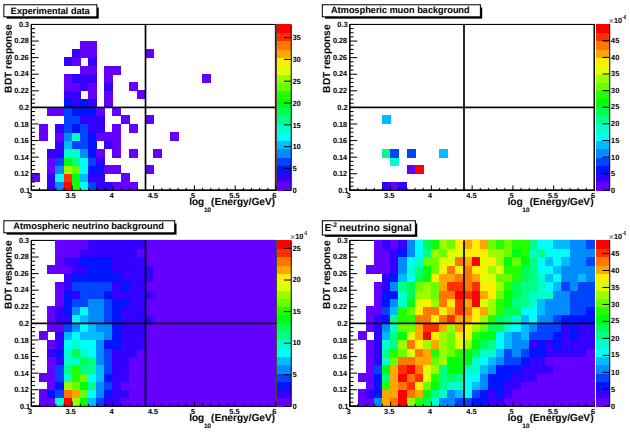

FIG. 9: The IceCube-40 level 6 BDT response and energy reconstructions, the four panels show the data, atmospheric muon background, atmospheric electron neutrino background, and E^{-2} spectrum electron neutrino signal. The level 6 cuts are shown by the black lines at BDT response = 0.2 and energy = 25 TeV. Events in the upper right quadrant were kept.

However, there may be some real signal events within the remaining data sample, so these must be treated carefully. Consequently, events lying far into the signal region of the parameter space were excluded from the optimisation. In the 10% burn sample of the data there were two events that lied in this signal region. These two signal events were excluded from the optimisation of the final level cut values. The analysis cuts were optimised based on the sensitivity and discovery potential of the final sample[29]. Figure 9 shows the BDT response cut and the energy cut for the data, simulated atmospheric muon background, simulated atmospheric electron neutrino background, and simulated E^{-2} spectrum electron neutrino signal.

The optimum cuts for the final level were BDT response $>$ 0.2 and energy $>$ 25 TeV. Figures 10(a) and 10(b) show the BDT response and energy distributions for the data, simulated atmospheric muon background, simulated atmospheric electron neutrino background, and simulated E^{-2} spectrum electron neutrino signal.

C. Systematic Uncertainties

The largest uncertainties in our analysis arise from our limited knowledge of the ice properties at the South Pole. Other small uncertainties arise from the DOM efficiencies, neutrino cross-sections, and the seasonal variation at the detector site. These sources of uncertainty are described below.

Flasher data from calibration runs is used to develop ice models by measuring absorption and scattering at different points throughout the ice with a known light source[10]. An ice model contains the depth, wavelength,

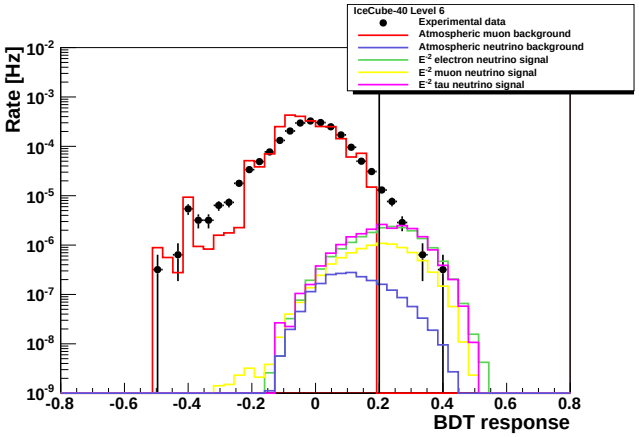

(a)BDT response $>$ 0.2.

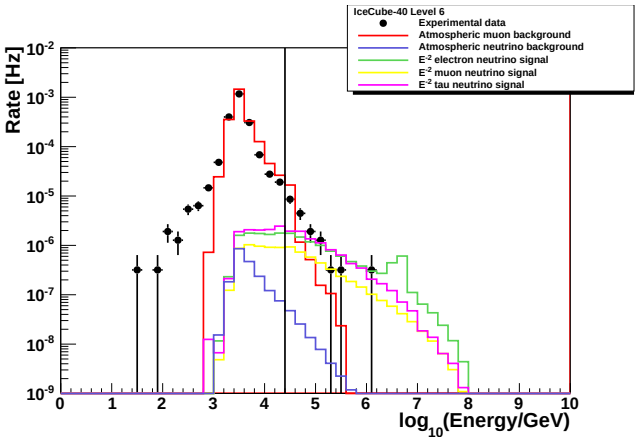

(b) Energy $>$ 25 TeV.

FIG. 10: The IceCube-40 level 6 filter, the data is shown by the black filled circles, simulated atmospheric muon background by the red line, simulated atmospheric electron neutrinos by the blue line, and simulated E^{-2} spectrum electron neutrino signal by the green line. The E^{-2} spectra for muon and tau neutrino simulations are shown in these plots by the yellow and magenta lines respectively.

and temperature dependent information throughout the detector and surrounding ice and bedrock. The model used in all simulations for this analysis was the *Additionally Heterogeneous Absorption* (AHA) model[10]. To carry out a study of the uncertainties arising from the ice model, simulated datasets were produced using an updated ice model. This model, called *South Pole ICE* (SPICE)[7], was developed after this analysis was complete. The systematic uncertainty from the ice models was $\pm$24.9% for E^{-2} neutrino spectrum signal, $\pm$17.8% for atmospheric neutrino background, and $\pm$12.4% for atmospheric muon background.

A DOMs efficiency is the ratio of the light collected by a DOM to the total light incident upon that DOM. The DOM efficiency includes the quantum efficiency of the PMT and the transmissivity of the optical gel and glass of each sphere. All DOMs in the IceCube-40 detector operated at $\pm$10% efficiency[3]. The systematic uncer-

tainty from the DOM efficiency was -0.1% $+12.6\%$ for E^{-2} neutrino spectrum signal and -11.7% $+17.2\%$ for atmospheric neutrino background.

This analysis used neutrino-nucleon cross-sections from HTEQ[25]. An alternative cross-section model is CSS[19] which was used for systematic studies. The systematic uncertainty from the neutrino cross-section model was $\pm 8.7\%$ for E^{-2} neutrino spectrum signal and $\pm 8.8\%$ for atmospheric neutrino background.

The atmosphere above the IceCube detector varies throughout the year. This is because of temperature and pressure variations in the layers of the Antarctic atmosphere[9]. The muon background simulation was generated assuming an October atmosphere because this is close to the average for the whole year. The systematic uncertainty from seasonal variations is $\pm 0.5\%$ for atmospheric muon background.

	E_ν^{-2} spectrum signal	Atm. neutrino background	Atm. muon background
Ice properties	$\pm 24.9\%$	$\pm 17.8\%$	$\pm 12.4\%$
DOM efficiencies	-0.1% $+12.6\%$	-11.7% $+17.2\%$	-
Cross-sections	$\pm 8.7\%$	$\pm 8.8\%$	-
Seasonal variation	-	-	$\pm 0.5\%$
Total	-26.4% $+29.2\%$	-23.0% $+26.3\%$	$\pm 12.4\%$

TABLE I: Systematic uncertainties for atmospheric muon background, atmospheric neutrino background, and E^{-2} spectrum neutrino signal simulations.

Table I shows a summary of the systematic uncertainties in this analysis. The total systematic uncertainty for each type of simulation is obtained by the square-root of the sum of the squares from each systematic source.

IV. RESULTS

After the event selection criteria were finalised the remaining 90% of the data was unblinded. The total live-time of the data for this analysis was 373.6 days.

The neutrino effective area $A_{\rm eff}^{\nu}(E_\nu, \theta)$ is the surface corresponding to 100% detection efficiency for neutrino detection. This includes contributions from event interaction probability, absorption in the Earth, propagation, neutrino cross-section, detection probability, and cut efficiencies. The efficiency of the detector can be represented by the effective area of the detector which we obtained by passing the simulated E^{-2} neutrino signal through all filtering levels of the analysis. Figure 11 shows the neutrino effective area for electron, muon, and tau neutrino signal.

The accuracy of the reconstruction algorithms was calculated from resolution plots of the simulated neutrino signal. These plots show the difference between the reconstructed value and the true simulated value of the reconstruction quantities. Figure 12 shows the energy resolution for this analysis. The fit is a Gaussian and gives a resolution value of 0.09 in log(energy).

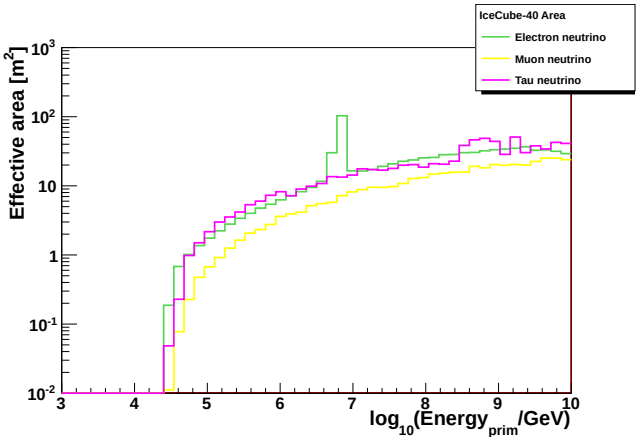

FIG. 11: IceCube-40 neutrino effective area as a function of primary neutrino energy. The three curves show electron, muon, and tau neutrino simulated signals. The peak in the electron neutrino curve corresponds to the Glashow resonance.

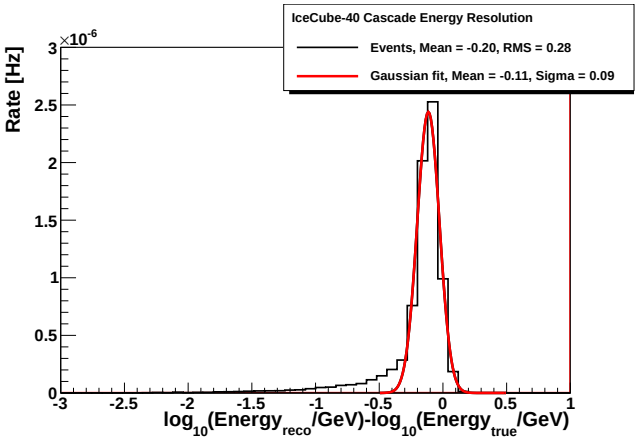

FIG. 12: Energy resolution, the red line is a Gaussian fit to the data which gives a resolution value of 0.09 in log(energy).

Event	Date of event	Time of event	Number of DOMs hit	BDT response	Reconstructed Energy (TeV)
1	18$^{\rm th}$ Apr 08	09:56:42	88	0.268	29.13
2	19$^{\rm th}$ Apr 08	04:48:26	139	0.375	30.81
3	23$^{\rm rd}$ Apr 08	01:23:14	194	0.416	175.28
4	10$^{\rm th}$ May 08	03:21:05	76	0.230	27.14
5	28$^{\rm th}$ May 08	23:54:42	103	0.225	41.36
6	5$^{\rm th}$ Jun 08	17:20:05	264	0.380	174.09
7	6$^{\rm th}$ Jul 08	21:54:24	81	0.293	31.20
8	30$^{\rm th}$ Aug 08	09:47:41	123	0.232	45.33
9	16$^{\rm th}$ Oct 08	11:32:47	359	0.236	144.20
10	8$^{\rm th}$ Nov 08	02:25:22	121	0.279	32.06
11	14$^{\rm th}$ Jan 09	20:43:29	82	0.203	46.83
12	6$^{\rm th}$ Feb 09	21:20:07	109	0.219	57.19
13	12$^{\rm th}$ May 09	13:03:25	98	0.295	39.88
14	17$^{\rm th}$ May 09	21:54:19	67	0.281	27.15

TABLE II: Summary of the observed events: date of event, time of event, number of DOMs hit, BDT response, and reconstructed energy.

We observed 14 cascade candidate events after event selection, on an expected background of $4.3^{+1.1}_{-1.0}$ atmospheric neutrino events and 7.7 ± 1.0 atmospheric muon events. The number of background events was estimated from the simulation of atmospheric muons and atmospheric neutrino events. Table II shows the 14 events, their date and time, the number of hit DOMs in the event, the BDT response, and the reconstructed energy.

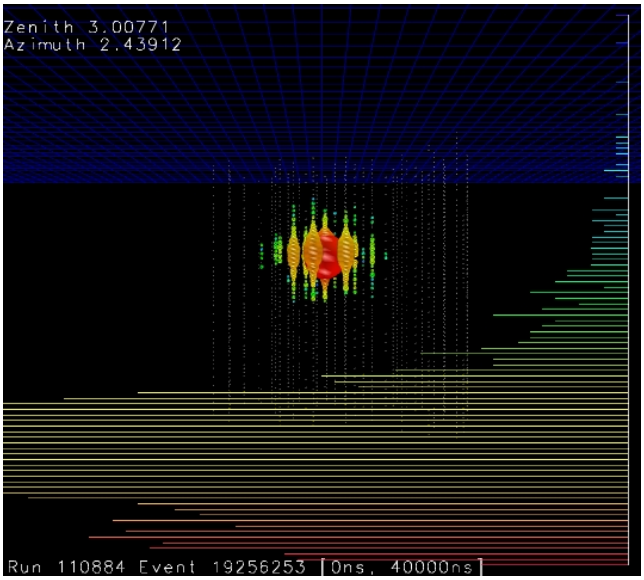

FIG. 13: An event that passed all event selection criteria. The DOMs are depicted as white circles forming the deployed IceCube strings. Every hit in the event is recorded as a coloured dot. The size of the coloured dots depicts the amount of charge received by that DOM, and the colour depicts the timing where red is earlier hits and blue is later hits. The charge and timing of the hits is also depicted along the right hand side of the event viewer display.

Figure 13 shows a cascade event from the data that passed all the event selection criteria. Here the DOMs are depicted by the white circles making up the IceCube-40 detector strings. The coloured circles represent the hits, where their size shows the size of the charge received by the DOM and their colours show the relative hit times. Red hits are early hits in the event and blue hits are late hits in the event. The charge and timing of the event is also depicted along the right side of the event viewer display. This event a BDT response of 0.416 and an energy of 175.28 TeV.

Figures 14(a) and 14(b) show the BDT response and energy spectra of the data, atmospheric muon background, atmospheric electron neutrino background, and E^{-2} spectrum all-flavour neutrino signal after unblinding. The 14 observed events can be seen above the final cut values of BDT response > 0.2 and energy > 25 TeV by the red vertical lines.

Using the 14 observed high energy cascade candidate events and a background of $4.3^{+1.1}_{-1.0}$ events from atmospheric neutrinos and 7.7 ± 1.0 events from atmospheric

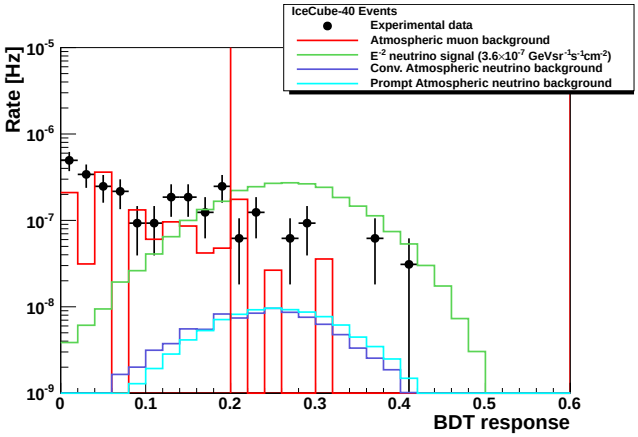

(a)BDT response spectrum.

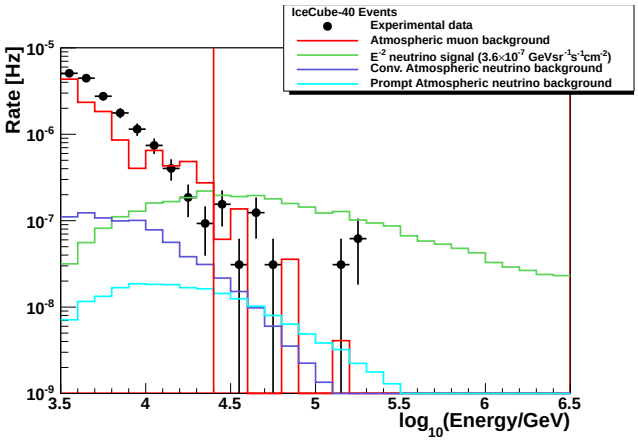

(b) Energy spectrum.

FIG. 14: The IceCube-40 BDT response and energy spectra after unblinding, the data is shown by the black filled circles, simulated atmospheric muon background by the red line, simulated atmospheric electron neutrinos by the blue lines, and simulated E^{-2} spectrum electron neutrino signal by the green line.

muons, we calculate a flux limit[29] using the TRolke method[34]. For an E^{-2} astrophysical neutrino spectrum and assuming a 1:1:1 flavour ratio at the Earth, the flux limit at a 90% confidence level is

$$\Phi_{\rm lim} E^2 \leq 5.21 \times 10^{-8} {\rm GeV sr}^{-1} {\rm s}^{-1} {\rm cm}^{-2}. \qquad (2)$$

The energy range for this calculation containing 90% of the signal is from 25 TeV to 5012 TeV. Figure 15 shows our limit. Model predictions are shown by the grey lines and analysis limits are shown by the coloured line with this analysis in black.

V. SUMMARY

We have reported on a high-energy search for astrophysical neutrino-induced cascades in the IceCube-40 detector. The data was taken between April 2008 and May 2009 with a total of 373.6 days livetime.

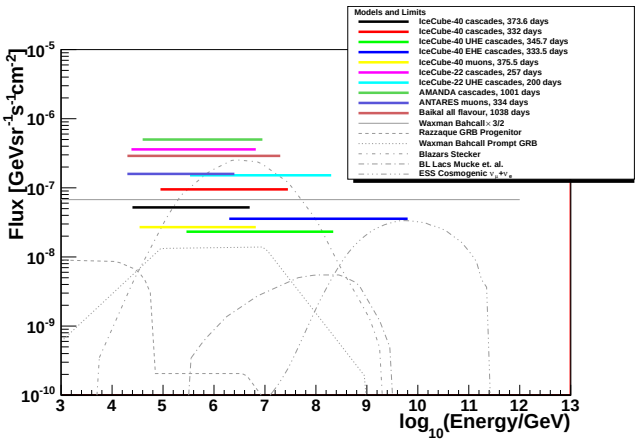

FIG. 15: IceCube analyses limits and model flux predictions. The analyses are shown by the coloured lines[1, 4–6, 8, 11, 20, 33, 38], with this analysis in black. The model predictions are shown by the grey lines[22, 37, 39, 40, 42, 43].

We observed 14 events on a background of $4.3^{+1.1}_{-1.0}$ atmospheric neutrino events and 7.7 ± 1.0 atmospheric muon events. We set a limit with a 90% confidence of $\Phi_{\rm lim} E^2 \leq 5.21 \times 10^{-8}\,{\rm GeV sr^{-1} s^{-1} cm^{-2}}$ on the astrophysical neutrino flux, assuming an E^{-2} spectrum and a 1 : 1 : 1 neutrino ratio at the Earth. In this limit 90% of the expected signal have energies in the range between 25 TeV to 5012 TeV.

This limit is below that reported from cascade searches using the IceCube-22 detector[6] and below the Waxman-Bahcall limit[43]. The IceCube detector is now completed with 86 strings and a volume of $1\,{\rm km}^3$. Future cascade searches will benefit from the larger effective area and a more favorable detector geometry which will lead improved cascade detection efficiency.

Acknowledgments

We acknowledge the support from the following agencies: U.S. National Science Foundation-Office of Polar Programs, U.S. National Science Foundation-Physics Division, University of Wisconsin Alumni Research Foundation, the Grid Laboratory Of Wisconsin (GLOW) grid infrastructure at the University of Wisconsin - Madison, the Open Science Grid (OSG) grid infrastructure; U.S. Department of Energy, and National Energy Research Scientific Computing Center, the Louisiana Optical Network Initiative (LONI) grid computing resources; National Science and Engineering Research Council of Canada; Swedish Research Council, Swedish Polar Research Secretariat, Swedish National Infrastructure for Computing (SNIC), and Knut and Alice Wallenberg Foundation, Sweden; German Ministry for Education and Research (BMBF), Deutsche Forschungsgemeinschaft (DFG), Research Department of Plasmas with Complex Interactions (Bochum), Germany; Fund for Scientific Research (FNRS-FWO), FWO Odysseus programme, Flanders Institute to encourage scientific and technological research in industry (IWT), Belgian Federal Science Policy Office (Belspo); University of Oxford, United Kingdom; Marsden Fund, New Zealand; Australian Research Council; Japan Society for Promotion of Science (JSPS); the Swiss National Science Foundation (SNSF), Switzerland.

[1] R. Abbasi, Y. Abdou, T. Abu-Zayyad, O. Actis, J. Adams, et al. Search for neutrino-induced cascades with five years of AMANDA data. *Astropart.Phys.*, 34:420–430, 2011.

[2] R. Abbasi et al. The IceCube Data Acquisition System: Signal Capture, Digitization, and Timestamping. *Nucl.Instrum.Meth.*, A601:294–316, 2009.

[3] R. Abbasi et al. Calibration and Characterization of the IceCube Photomultiplier Tube. *Nucl.Instrum.Meth.*, A618:139–152, 2010.

[4] R. Abbasi et al. A Search for a Diffuse Flux of Astrophysical Muon Neutrinos with the IceCube 40-String Detector. *Phys.Rev.*, D84:082001, 2011.

[5] R. Abbasi et al. Constraints on the Extremely-high Energy Cosmic Neutrino Flux with the IceCube 2008-2009 Data. *Phys.Rev.*, D83:092003, 2011.

[6] R. Abbasi et al. First search for atmospheric and extraterrestrial neutrino-induced cascades with the IceCube detector. *Phys.Rev.*, D84:072001, 2011.

[7] R. Abbasi et al. Study of South Pole ice transparency with IceCube flashers. 2011. Papers submitted by the IceCube Collaboration to the 32nd International Cosmic Ray Conference, Beijing 2011/ part VI.

[8] R. Abbasi et al. A Search for UHE Tau Neutrinos with IceCube. 2012.

[9] M. Ackermann and Elisa Bernardini. An investigation of seasonal variations in the atmospheric neutrino rate with the AMANDA-II neutrino telescope. 2005.

[10] M. Ackermann et al. Optical properties of deep glacial ice at the South Pole. *Geophys.Res.*, 111(D13203):282–300, 2006.

[11] J.A. Aguilar et al. Search for a diffuse flux of high-energy ν_μ with the ANTARES neutrino telescope. *Phys.Lett.*, B696:16–22, 2011.

[12] H. Athar, M. Jezabek, and O. Yasuda. Effects of neutrino mixing on high-energy cosmic neutrino flux. *Phys.Rev.*, D62:103007, 2000.

[13] G.D. Barr, T.K. Gaisser, P. Lipari, Simon Robbins, and T. Stanev. A Three - dimensional calculation of atmospheric neutrinos. *Phys.Rev.*, D70:023006, 2004.

[14] John F. Beacom, Nicole F. Bell, Dan Hooper, Sandip Pakvasa, and Thomas J. Weiler. Measuring flavor ratios of high-energy astrophysical neutrinos. *Phys.Rev.*, D68:093005, 2003.

[15] R. Brun and F. Rademakers. ROOT: An object oriented data analysis framework. *Nucl.Instrum.Meth.*, A389:81–

86, 1997.

[16] D. Chirkin and W. Rhode. Muon Monte Carlo: A new high precision tool for muon propagation through matter. pages 15–22, 2002.

[17] Dmitry Chirkin. Fluxes of atmospheric leptons at 600-GeV - 60-TeV. 2004.

[18] Dmitry Aleksandrovich Chirkin. Cosmic ray energy spectrum measurement with the Antarctic Muon and Neutrino Detector Array (AMANDA). 2003.

[19] Amanda Cooper-Sarkar and Subir Sarkar. Predictions for high energy neutrino cross-sections from the ZEUS global PDF fits. *JHEP*, 0801:075, 2008.

[20] Zh.A. Dzhilkibaev. Search for a diffuse flux of high-energy neutrinos with the Baikal neutrino telescope NT200. 2009.

[21] Rikard Enberg, Mary Hall Reno, and Ina Sarcevic. Prompt neutrino fluxes from atmospheric charm. *Phys.Rev.*, D78:043005, 2008.

[22] Ralph Engel, David Seckel, and Todor Stanev. Neutrinos from propagation of ultrahigh-energy protons. *Phys.Rev.*, D64:093010, 2001.

[23] Gary J. Feldman and Robert D. Cousins. A Unified approach to the classical statistical analysis of small signals. *Phys.Rev.*, D57:3873–3889, 1998.

[24] Y. Freund and R.E. Schapire. A decision-theoretic generalization of on-line learning and an application to boosting. *Journal of Computer and System Sciences*, 55:119–139, 1997.

[25] Raj Gandhi, Chris Quigg, Mary Hall Reno, and Ina Sarcevic. Ultrahigh-energy neutrino interactions. *Astropart.Phys.*, 5:81–110, 1996.

[26] Askhat Gazizov and Marek P. Kowalski. ANIS: High energy neutrino generator for neutrino telescopes. *Comput.Phys.Commun.*, 172:203–213, 2005.

[27] R. Glasstetter et al. Analysis of electron and muon size spectra of EAS. 1999.

[28] D. Heck, G. Schatz, T. Thouw, J. Knapp, and J.N. Capdevielle. CORSIKA: A Monte Carlo code to simulate extensive air showers. 1998.

[29] Gary C. Hill and Katherine Rawlins. Unbiased cut selection for optimal upper limits in neutrino detectors: The Model rejection potential technique. *Astropart.Phys.*, 19:393–402, 2003.

[30] Anthony M. Hillas. Cosmic Rays: Recent Progress and some Current Questions. 2006.

[31] Andreas Hocker, Peter Speckmayer, Jorg Stelzer, Fredrik Tegenfeldt, and Helge Voss. TMVA, toolkit for multivariate data analysis with ROOT. pages 184–187, 2007.

[32] Joerg R. Hoerandel. On the knee in the energy spectrum of cosmic rays. *Astropart.Phys.*, 19:193–220, 2003.

[33] H. Johansson. Searching for an Ultra High-Energy Diffuse Flux of Extraterrestrial Neutrinos with IceCube 40. 2012. Ph.D. Thesis in preparation (Advisor: Walck, Christian).

[34] J. Lundberg, J. Conrad, W. Rolke, and A. Lopez. Limits, discovery and cut optimization for a Poisson process with uncertainty in background and signal efficiency: TRolke 2.0. *Comput.Phys.Commun.*, 181:683–686, 2010.

[35] Johan Lundberg, P. Miocinovic, T. Burgess, J. Adams, S. Hundertmark, et al. Light tracking for glaciers and oceans: Scattering and absorption in heterogeneous media with Photonics. *Nucl.Instrum.Meth.*, A581:619–631, 2007.

[36] Predrag Miocinovic. Muon energy reconstruction in the Antarctic Muon and Neutrino Detector Array (AMANDA). 2001.

[37] A. Muecke, R.J. Protheroe, R. Engel, J.P. Rachen, and T. Stanev. BL Lac Objects in the synchrotron proton blazar model. *Astropart.Phys.*, 18:593–613, 2003.

[38] S. Panknin. Search for Neutrino-Induced Cascades with the IceCube Neutrino Detector. 2011. Ph.D. Thesis in preparation (Advisor: Kowalski, Marek).

[39] Soebur Razzaque, Peter Meszaros, and Eli Waxman. Neutrino tomography of gamma-ray bursts and massive stellar collapses. *Phys.Rev.*, D68:083001, 2003.

[40] Floyd W. Stecker. A note on high energy neutrinos from agn cores. *Phys.Rev.*, D72:107301, 2005.

[41] Bernhard Voigt. Sensitivity of the IceCube Detector for Ultra-High Energy Electron-Neutrino Events. 2008.

[42] Eli Waxman and John N. Bahcall. High-energy neutrinos from cosmological gamma-ray burst fireballs. *Phys.Rev.Lett.*, 78:2292–2295, 1997.

[43] Eli Waxman and John N. Bahcall. High-energy neutrinos from astrophysical sources: An Upper bound. *Phys.Rev.*, D59:023002, 1999.